Coupled electronic and nuclear dynamics at interfaces of artificial photosynthesis devices

Haas, T. de

Citation

Haas, T. de. (2025, September 4). *Coupled electronic and nuclear dynamics at interfaces of artificial photosynthesis devices*. Ridderprint, Leiden. Retrieved from https://hdl.handle.net/1887/4259657

Chapter 3: Strategies to Enhance the Rate of Proton-Coupled Electron Transfer Reactions in Dye-Water Oxidation Catalyst Complexes

Excited state calculations on two supramolecular catalyst-dye complexes for water oxidation reveal an avoided crossing in the region of the transition state for the rate-limiting proton coupled electron transfer steps. Two strategies are discussed to exploit this excited state energy landscape to accelerate the water splitting process.

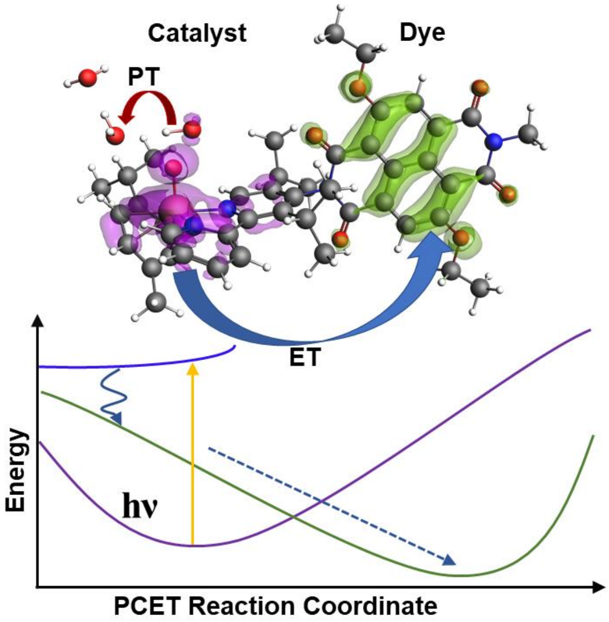

This chapter is based on:

T. de Haas, H. van Overeem, H.J.M. de Groot, F. Buda. Strategies to Enhance the Rate of Proton-Coupled Electron Transfer Reactions in Dye-Water Oxidation Catalyst Complexes. *ChemPhotoChem* **2023**, e202200274.

Chapter 3: Strategies to Enhance the Rate of Proton-Coupled Electron Transfer Reactions in Dye-Water Oxidation Catalyst Complexes

3.1 Abstract

A thorough understanding of the Proton Coupled Electron Transfer (PCET) steps that are involved in photocatalytic water oxidation is of crucial importance to increase the efficiency of dye-sensitized photoelectrochemical cells (DS-PEC) for solar to fuel conversion. This work provides a computational investigation of the ground and excited state potential energy surfaces of PCET reactions in two supramolecular dye-catalyst complexes for photocatalytic water splitting. The Intrinsic Reaction Coordinate path is computed for the rate limiting PCET step in the catalytic cycle for both complexes. Using time-dependent density functional theory calculations, it is shown that the ground and excited state potential energy surfaces have a near-degeneracy in the region of the PCET transition state. We discuss two possible strategies that take advantage of this feature to accelerate the PCET reaction: (i) through optimizing the conditions for vibronic coupling by chemical design and synthesis or (ii) through populating the product state with appropriately tuned laser pulses.

3.2 Introduction

The increase of carbon dioxide levels in the earth's atmosphere, a by-product of the combustion process of fossil fuels, has shown to be one of the driving forces behind global warming. To reduce the fierce consequences of climate change, the world has to turn entirely to environmentally benign resources of energy within the next three decades.[1] Dye-Sensitized Photoelectrochemical Cells (DS-PECs) are a promising instrument to contribute to the transition towards net zero carbon emissions.[2] These devices harness the technology to convert solar-light and water directly into hydrogen gas by integrating the photovoltaic (PV) and electrochemical process in a single cell, thereby reducing overpotential and current losses of a decentralized PV and electrocatalytic process.[3,4] At the heart of a DS-PEC device lays the process of photo-induced water oxidation. In this sunlight-driven catalytic reaction, two water molecules are converted into molecular oxygen, four protons and four electrons in a series of four Proton Coupled Electron Transfer (PCET) steps. Each PCET step is initiated by photoinduced electron transfer from a light-absorbing dye to an anode, usually TiO_2. Subsequently, bidirectional PCET takes place at the Water Oxidation Catalyst (WOC), where the electron moves to the dye and the proton transfers to the water environment.

In the recent decades substantial progress has been made in the development of catalysts that can facilitate the water splitting reaction.[5–7] Generally, two classes of WOC's can be distinguished[8], WOC's that operate via the mononuclear Water Nucleophilic Attack (WNA) pathway[9–12] and WOC's that operate via the binuclear interaction of two metal centers (I2M) pathway.[13–17] In the WNA mechanism, the rate determining (PCET) step is the nucleophilic attack of a solvent water molecule on the metal-oxo species at the centre of the catalyst and simultaneous O-H dissociation to form a high-energy peroxo-intermediate and a hydronium ion. In the I2M mechanism, the formation of this intermediate is circumvented by forming the O-O bond directly from two metal-oxo species in an intermolecular fashion.[18,19] Although remarkable turnover frequencies have been reported with WOC's that work via I2M,[13,14] it remains questionable whether this type of mechanism would still apply once the molecular catalyst is immobilized on a surface in a DS-PEC device. Therefore, also research into the optimization of the WNA mechanism is important.

Often, PCET reactions can proceed over a non-adiabatic path, coupling reactant and product adiabatic electronic states.[20–23] Inclusion of vibronically excited states in calculations is critical for recovering experimental data from computations.[24] Earlier studies in our group have shown that nuclear modes that are resonant with electronic motion can enhance non-adiabatic coupling between the reactant and product states, opening a channel between such states for deterministic charge transfer at high yield, beyond adiabatic practices where yields are limited by back reaction and recombination losses.[3] In order to engineer systems for artificial photosynthesis with a near unity quantum yield, taking into account properly the interplay between nuclear and electronic motion will thus be of crucial importance. In a recent study from our group, it was shown that vibronic coupling plays a central role in the rate limiting O-O bond forming PCET step in a WOC-dye complex.[25,26] In particular, it was shown that a specific torsional motion was coupled to the electron transfer (ET) process. Through rational functionalization of the catalyst ligand backbone, the characteristic frequencies associated with this mode were tuned to achieve faster charge transfer.

Interesting advances have been made in exploiting non-adiabatic decay pathways to trigger PCET events.[27–31] Recently, Schlenkler et al. showed that PCET between trianisole-heptazine and a series of phenol-derivatives can selectively be controlled by irradiating the complex in solution with laser pulses.[32] The driving force for this reaction is the result of the intermolecular charge transfer excitation from the phenol to the heptazine core. Ab initio non-adiabatic molecular dynamics (AIMD) simulations indicate that a H-atom can be extracted from water using laser irradiation with the trianisole-heptazine complex.[33] Although this type of hydrogen atom abstraction (HAT) mechanism is different from the bidirectional

PCET steps that take place in water-oxidation, it represents a new paradigm in reactivity with promise for solar fuel production.

The challenge is now to design artificial photosynthesis systems that can optimally exploit these non-adiabatic phenomena for PCET reactions. With this goal in mind, we have computationally explored the ground and excited state potential energy surfaces for different catalyst-dye models for photocatalytic water oxidation.

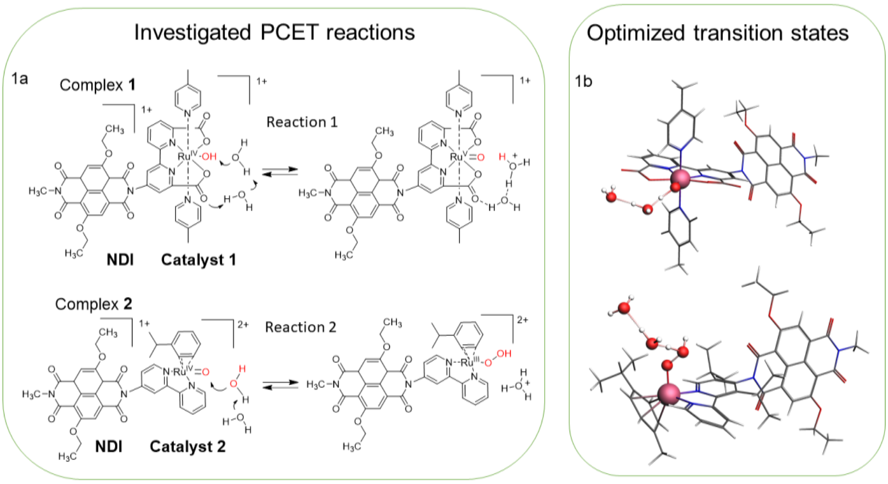

Figure 3.1. *A schematic depiction of the investigated reaction steps for complex 1 (**1**) and complex 2 (**2**) are provided in (a). Earlier work has shown that these two reaction steps are thermodynamically the most demanding steps in the water oxidation cycle for these two catalysts.*[25,34] *The local charge on the WOC, dye and proton accepting water molecule are also indicated. For both complexes the overall charge is conserved over the reaction, but locally a plus charge moves from the NDI to the excess solvated proton. (b) Shows the optimized transition states for **1** and **2**. The transition state structures clearly show the formation of a hydrogen bonded water molecules chain to distribute the excess charge.*

The general outline of this chapter is as follows: In the first section, the generation of the PCET reaction path using the Intrinsic Reaction Coordinate (IRC)[35,36] method is discussed. Then, it is demonstrated that the electron and hole transfer along the obtained reaction path can be followed by plotting the spin-density. In the subsequent section the excited state potential energy surface along the generated reaction path is analysed. To this end, time dependent DFT (TDDFT) and spin-flip TDDFT (SF-TDDFT) were employed. Normal TDDFT fails to properly describe regions of strong coupling, due to the multiconfigurational nature of the electronic ground state. Instead, in SF-TDDFT both ground and excited states are treated as spin-flip excitations from a state with different multiplicity. Hence this single determinant method is able to describe near degeneracies and conical intersections.[37–39] It has been demonstrated that SF-TDDFT can describe dissociation reactions, avoided crossings and conical intersections reasonably well, and with a relatively low computational cost.[40–44] For both investigated photo-induced PCET steps, a conical intersection is found between the ground state and a higher lying excited state in the region near the transition state. A discussion is provided on plausible strategies to exploit this characteristic energy landscape, either by appropriately shaped laser pulses as done in the emerging field of optochemistry[45], or through optimizing the resonance conditions for vibronic coupling by synthetically tuning molecular properties, with the goal of reducing back-reaction and recombination losses.[46]

3.3 Results and Discussion

3.3.1 Search for the PCET reaction path using the Intrinsic Reaction Coordinate method

Two particular ruthenium based catalysts are considered, $[Ru^{II}(bda)(pic)_2(H_2O)]^+$ (bda = 2,2′-bipyridine-6,6′-dicarboxylic acid, pic = 4-picoline; Figure 3.1a, catalyst 1) and $[(cy)Ru^{II}bpy(H_2O)]^{2+}$ (cy = p-cymene, bpy = 2,2’-bipyridine; Figure 3.1a, catalyst 2), which operate via the I2M and WNA mechanism, respectively.[11,13,47] 2,6-diethoxy-1,4,5,8-diimidenapthalene (Figure 3.1a, NDI) was selected as the light absorbing dye. The redox and light absorbing properties of this specific NDI dye, and other core substituted derivatives, have been investigated extensively.[48–50] Recent computational investigations have shown that this molecule has suitable absorption and redox properties to drive the four PCET steps that are required to complete the water oxidation process.[25,51] The dye was considered to be covalently bound to the WOC via the nitrogen atom as depicted in Figure 3.1. For the remainder of this paper, the bound WOC-Dye complexes in Figure 3.1a will be referred to as **1** and **2**. Coupling of the dye via the non-substituted carbon atom at the naphthalene core was also considered. As this case yielded results very similar to the other binding mode, the obtained results for that system are provided in the appendix (see appendix, 3A.1.1 In order to properly describe the solvation of the hydronium cation after each PCET step, explicit water molecules were included in the model system, *i.e.* two water molecules for **1** and three water molecules for **2** (Figure 3.1b). Addition of explicit water stabilizes the product significantly, as it allows for the formation of a Zundel cation. Taking into account the WOC, the dye and explicit water molecules, allows for a study of the entire PCET process after photo-oxidation of the dye. The TiO_2 semiconductor surface is not considered explicitly as previous work has shown that the photo-induced electron injection process from the NDI to the conduction band of TiO_2 is fast compared to the water oxidation reaction timescale.[52] The systems are thus optimized in their oxidized form ($[WOC]^{+}$-$dye^{\bullet+}$ for **1**, and $[WOC]^{2+}$-$dye^{\bullet+}$ for **2**). For both complexes, the catalytic step that was shown to be thermodynamically most demanding has been investigated. Earlier work has shown that for **1**, this involves a PCET step where the proton transfers from the Ru(IV)-hydroxo intermediate to bulk water[13,34] (Figure 3.1a, reaction 1) and for **2** this involves the O-O bond formation via the WNA mechanism (Figure 3.1a, reaction 2).[11,25]

For both WOC-dye complexes, a transition state (TS) was located, and its saddle point character was verified with vibrational analysis. For the TS of **1**, the imaginary normal mode features the displacement of the proton from the OH ligand to the nearest water molecule (see Figure 3.1b, top). In the case of **2**, the

TS captures both the formation of the O-O bond and simultaneous release of the proton to the bulk water (see Figure 3.1b, bottom). Starting from the optimized TS, a ground state IRC path was generated, which corresponds to a minimum energy path in mass-weighed coordinates.[35,36] The IRC paths feature a Grotthuss-type mechanism for the proton diffusion to the solvent water (xyz trajectory files of the IRC paths can be found as supplementary material to the original publication).[53,54] For **1**, the IRC calculations yield a reaction path in which the ruthenium hydroxide O-H bond is broken and the hydronium is subsequently stabilized by coordinating to the carboxylate group of the bda^{2-} ligand. It will be interesting to further investigate if the stabilizing role of the ligand in this catalytic cycle is consistently observed when explicit solvation is included in AIMD. The IRC for **2** yields a path involving simultaneous O-O bond formation and O-H bond dissociation to form a hydronium cation. In this system, the propagation of the IRC path converged when the O-O distance was elongated from 1.75 Å in the TS, to 2.05 Å in the reactant geometry. To obtain a comprehensive picture of the water molecule approaching the Ru-OXO species, the IRC path was extended with a series of ten constrained geometry optimizations in which the O-O bond length was increased stepwise. Detailed descriptions of the procedures used to obtain the reaction paths, the obtained xyz trajectory files and the ground state energy profile are provided in the appendix, 3A.2.2.

3.3.2 Tracking the electron transfer during the PCET reaction

The obtained IRC paths were used as input structures for DFT calculations with the hybrid B3LYP functional, to study ET along the PCET reaction. Due to the presence of unpaired electrons in the ground state, ET can be analyzed by visualizing the spin density. The spin densities of **1** and **2**, in the reactant and product geometries, are depicted in Figure 3.2. For **1**, the unpaired electron is initially localized on the NDI, as a result of the excited state electron injection into the TiO_2 semi-conductor. After proton transfer, the whole spin density is transferred to the catalyst, indicating that the catalyst has been oxidized leading to electron pairing on the NDI (($[\mathrm{WOC}]^{+}$-dye$^{\bullet +}$ → $[\mathrm{WOC}]^{\bullet 2+}$-dye). The situation for **2** is slightly different. Although a doublet multiplicity is imposed over the entire reaction path, **2** has three unpaired electrons after electron injection into the semi-conductor: specifically, two unpaired electrons on the catalyst and one unpaired electron with opposite spin on the NDI (see Figure 3.2, bottom left). In Figure 3.2 it is seen that after the PCET step, **2** has only one unpaired electron on the WOC in the product structure. Further investigations show that the S=3/2 and S=1/2 states in the reactant geometry are nearly degenerate ($\Delta E < 0.01$ kcal mol^{-1}), which is plausible since the ruthenium center and the NDI are spatially separated by about 5 Å. This quasi degeneracy is also the reason for serious spin contamination in the calculations on these initial structures. The expectation value for the $\hat{S}^2$ operator is about 1.77 for the reactant structure of **2**, while a pure S=1/2 state would yield a value of 0.75 for this operator and a pure S=3/2 state would yield a value of 3.75. The α and β spin density are, however, localized exclusively on the WOC and NDI respectively, corresponding to the expected electronic state in which a local triplet is formed on the WOC and a local doublet on the NDI. The spin contamination disappears as soon as the S=3/2 and S=1/2 degeneracy is lifted. Nevertheless, we note that the spin contamination could still affect the obtained energies.[55] A figure with the $\hat{S}^2$ expectation value plotted over the reaction coordinate is provided in the appendix (3A.2.3, Figure 3A.7).

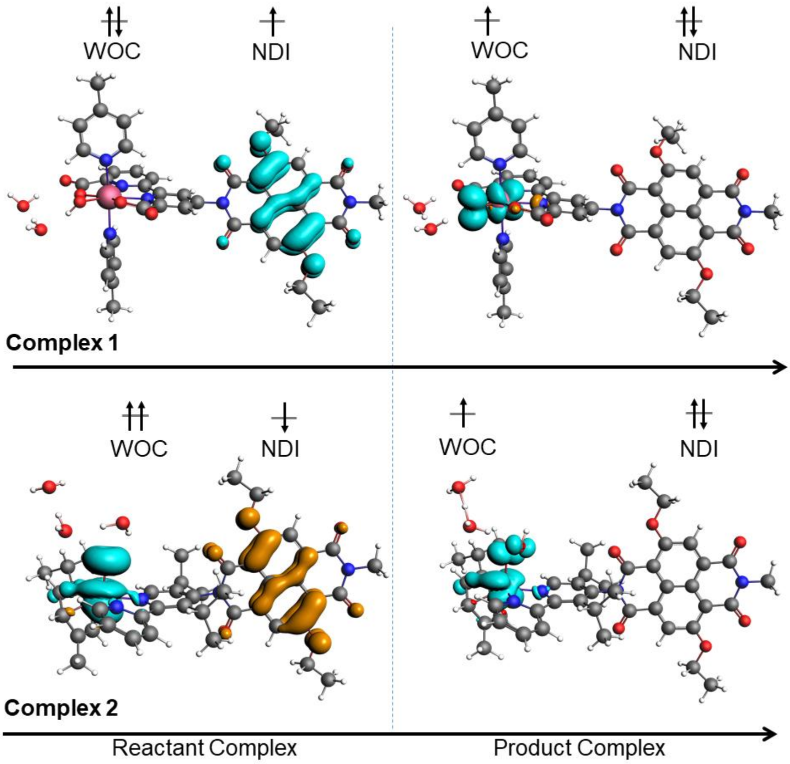

Figure 3.2. *Reactant and product geometries of* ***1*** *and* ***2*** *obtained with the IRC method at the OPBE/TZP/COSMO level of theory. The spin densities have been calculated at the B3LYP/TZ2P/COSMO level of theory and the isosurface value was set at 0.002. The schematic electronic configurations with the unpaired electrons are indicated. Cyan corresponds to spin up and orange corresponds to spin down electrons. Although for both systems the overall charge is conserved over the entire reaction path, locally a plus charge moves from the NDI to the excess solvated proton.*

3.3.3 Exploring the excited state potential energy surfaces with TDDFT

With the aim of gaining insights into the excited state potential energy surfaces along the obtained IRC reaction coordinates, TDDFT was employed. Excited state calculations were performed on a selection of structures along the IRC path. In

Figure 3.3, the ground state and excited state profile for the two systems are projected along a specific geometrical parameter that represents the main bonding rearrangement during the PCET step. For **1**, the selected reaction coordinate is the difference between the O_I-H and the O_{II}-H distances, with O_I being the oxygen of the OH ligand and O_{II} the oxygen of the proton acceptor water molecule (see inset in Figure 3.3, upper panel). For **2**, the selected reaction coordinate is the difference between the O_I-O_{II} and the O_{II}-H distances, with O_I being the oxygen of the oxo ligand and O_{II} the oxygen of the attacking water molecule (see inset in Figure 3.3, lower panel).

AIMD simulations on **2** in explicit solvation have convincingly shown that reaction 2 is exothermic upon photo-oxidation of the NDI.[25,26] It is noted that in these static calculations the ground state reaction (red line in Fig. 3) is endothermic. Given the fact that an implicit solvation model is used with only a few explicit water molecules and that the IRC method does not necessarily yield a fully optimized structure, it is plausible that these calculations underestimate the stability of the solvated hydronium cation in the product structure. Nevertheless, this will not affect the main conclusions of this work, as we are here primarily interested in exploring the behavior of the ground and excited state energy profile along the reaction coordinate, especially in the region of near degeneracy.

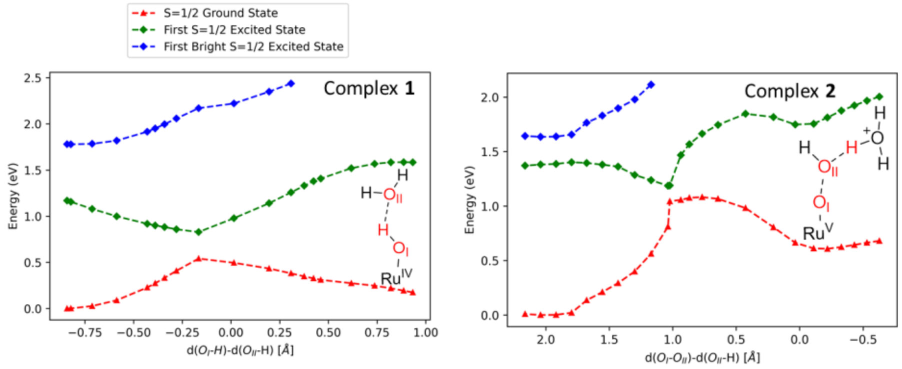

Figure 3.3. *The obtained S=1/2 ground state (red), first S=1/2 excited state (green) and "bright" S=1/2 excited state (blue) potential energy surfaces along the reaction coordinates for the rate determining PCET step of **1** (top) and **2** (bottom). The energy for the ground state and the first excited states for each point is evaluated at the B3LYP/TZ2P/COSMO level of theory within the TDDFT framework.*

The calculations reveal an avoided crossing between the ground state and first excited state at the PCET transition state for **1**. Also **2** moves through an avoided crossing, yet a key difference is that this crossing does not completely coincide with the transition state for the PCET reaction. The reason for this is that the reaction coordinate involves two molecular rearrangements, namely, formation of the O-O bond and dissociation of the O-H bond. Conversely, the PCET step investigated in **1** involves only proton transfer from the ruthenium hydroxo species to the water environment. Additionally, it is also observed that the barrier for the rate determining step of the reaction with **1** is significantly lower than the rate determining step for the reaction with **2** (*ca*. 13 kcal mol^{-1} against 20 kcal mol^{-1} evaluated at the B3LYP/TZ2P/COSMO level of theory). This is in agreement with prior studies that have shown the catalyst in **1** to have higher turnover frequencies than the catalyst in **2**.[11,13] It is noted that the B3LYP/TZ2P setup here estimates a barrier significantly higher than the OPBE/TZP/COSMO calculations (>7 kcal mol^{-1} for both complexes, see appendix, 3A.2.2). It is emphasized again that our calculations are not aimed at precisely estimating reaction rates. In addition to the analysis of the excited state profile along the ground state PCET reaction coordinate, also an excited state geometry relaxation was performed from the Franck-Condon point at the reactant structure of **1**. These calculations are discussed in the appendix, 3A.1.4.

To gain further insights into the characteristics of the ground and excited state, the Natural Transition Orbitals (NTOs) at the reactant and product geometries for **1** and **2** are depicted in Figure 3.4. NTOs are a practical way of transforming the transition density matrix to obtain a set of compact orbitals that describe the transitions of interest in as few as possible terms.[56] Starting from the reactant complex, it was found that the first excited state of the oxidized complex corresponds to a charge transfer excitation from the catalyst to the NDI, for both **1** and **2**. Then, in the product structure, again for both investigated complexes, the first excited state is described as a charge transfer excitation from the dye to the catalyst. Instead of mixing of the involved NTOs prior to approaching the avoided crossing, a sudden rearrangement is observed upon moving over the barrier. For the reactant and product structures of **1**, the occupied and virtual NTO's correspond entirely to the spin α HOMO and LUMO. For the product structure of **2**, this is also the case. The observed transitions correspond for >99.5% to the HOMO-LUMO excitation. For the reactant structure of **2**, the HOMO-LUMO orbital excitation constitutes 96.1% of the displayed transition.

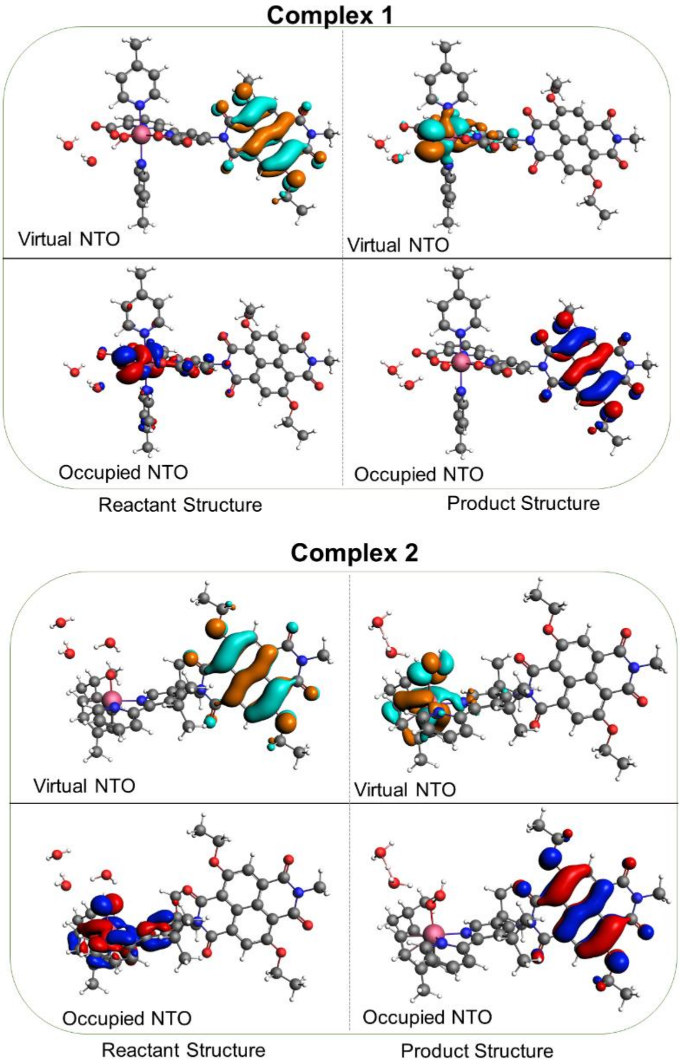

Figure 3.4. *The Natural Transition Orbitals (NTO's) of the first excitation, calculated at the B3LYP/TZP/COSMO level of theory on the reactant and product geometries of **1** (top) and **2** (bottom). It is observed that for the reactant structure, the first excited state is a charge transfer excitation from the ruthenium catalyst to the NDI, while for the product structure, the excitation corresponds to a charge transfer from the NDI to the ruthenium center.*

One strategy to optimize PCET steps in artificial photosynthetic systems is to utilize the interplay between nuclear and electronic motion. Interestingly, our calculations sketch a potential energy landscape where the ground and excited state get within a 0.4 eV energy gap, which is the typical domain of molecular vibrational energies. This indicates that in these systems the two electronic states could be coupled vibronically, if a nuclear mode is available with the appropriate vibrational frequency. Earlier constrained AIMD simulations in our group have shown that electron transfer in **2** is strongly inhibited once the C-N-C-C torsional mode at the WOC-dye interface is fixed.[25,26] The results presented in this paper provide a rationale behind this observation: The energy gap between the two adiabatic states in the region of the transition state is around 0.1 eV, which is indeed comparable to the energy associated with the torsional mode discussed in ref.[26] The resonance between the torsional mode frequency and the electronic energy gap between the reactant and product states, leads to a deterministic conversion pathway from the reactant to the product. These results show that vibronic coupling is an important mechanistic aspect to consider, to properly understand the catalytic performance of artificial photosynthetic devices.

In a recent publication, Schlenkler and co-workers have shown that PCET between a series of phenol and heptazine derivatives can be driven and controlled using laser pulses.[32] The authors use quantum chemical calculations to show that the probed decay process involves excitation to a short lived excited state and subsequent population of a charge transfer state. In this article, we argue that this idea can be extended to catalyst-dye complexes that are useful for water oxidation. The results in Figure 3.3 highlights two important observations. The first is that only two electronic states are relevant for the ET transfer, the reactant state, where the electron is still on the catalyst, and the product state, where the unpaired electron is transferred to the NDI. This implies that the product state could be accessed by exciting the systems at their reactant geometry. Second, for both complexes, the product state PES in the geometry corresponding to the reactant has a gradient towards the product geometry. These observations support the idea that the PCET reaction can be initiated by irradiating the complex solution with appropriately tuned laser pulses, accelerating the reaction and preventing back reaction.

To explore this idea in more detail, the oscillator strengths between the ground state and higher lying excited states were assessed. The excitation energies and oscillator strengths at the reactant and product geometries for **1** and **2** are given in the appendix, 3A.3.1, table 3A.2 and 3A.3. Additionally, we have also examined the coupling between reactant and product states based on the generalized Mulliken-Hush ansatz. This analysis is provided in the appendix, 3A.3.2.[57,58] Similar to the work of Schlenkler *et al.*, the charge transfer state that triggers PCET is optically dark. This would imply that once this state is populated, it will be unlikely that it will decay to the ground state through light emission. The first bright excitation from the ground state is found at 1.78 eV (number 7, 3A.3.1 table 3A.2) for **1** and at 1.63 eV (number 5, 3A.3.1 table 3A.3) for **2** at their initial structures on the computed reaction paths (see also table 3A.2 and 3A.3 and Figure 3.3, the first bright S=1/2 excited state). The calculations do not provide information on radiative or non-radiative decay pathways from these states to the first S=1/2 excited state. Ab initio non-adiabatic molecular dynamics simulations could provide insights into non-radiative pathways, while radiative pathways could be explored by calculating oscillator strengths between excited states.

The region around the avoided crossing was further investigated with SF-TDDFT. In traditional TDDFT, the ground state is optimized self-consistently, opening the gap between occupied and unoccupied orbitals. In the spin-flip approach, a state of different spin symmetry than the ground state is self-consistently optimized and used subsequently as a reference, to obtain the ground state and excited states electronic configurations of interest, by a spin-flip excitation. In Figure 3.5, the diabatic potential energy surfaces obtained with SF-TDDFT are plotted along the same reaction coordinates used for Figure 3.3. For both systems, a diabatic relaxation pathway (green line) is found along the PCET reaction coordinate.

Spin-flip excitations to the *S*=1/2 ground and *S*=1/2 excited states are calculated from the *S*=3/2 reference state, which is also shown in grey in Figure 3.5. Notice that this is not the same state as the *S*=1/2 'bright state' that was found earlier with TDDFT, shown in Figure 3.3.

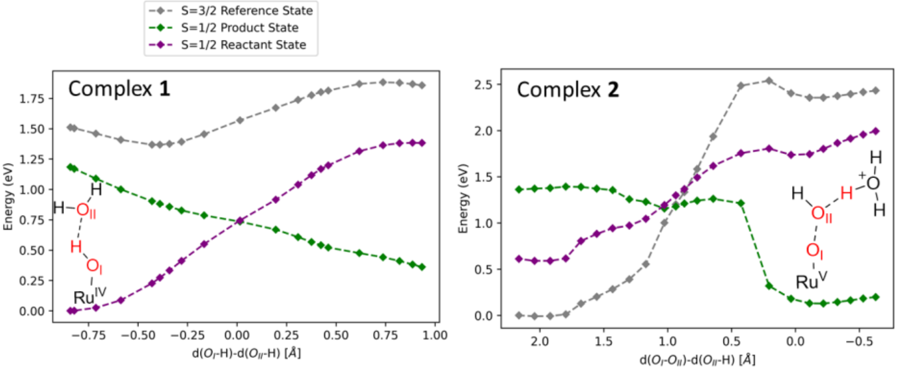

Figure 3.5. *SF-TDDFT potential energy surfaces along the reaction coordinates for the rate determining PCET step of **1** (top) and **2** (bottom). A clear intersection is observed for the reactant (purple) and product (green) states. The S=3/2 reference state is also reported in grey. The energy for the reactant and product states is evaluated at the B3LYP/TZ2P/COSMO level of theory.*

Both the reactant and product state yield a smooth energy profile when calculated as a spin-flip excitation from the *S*=3/2 reference state (dots in grey) in **1**. The *S*=3/2 reference state was found to be energetically separated by at least 0.3 eV from the investigated *S*=1/2 ground and excited states, along the entire reaction path. Also, the smoothness of the curve indicates that the same electronic configuration is retained. As was discussed earlier in this work, we know that for **2** the lowest *S*=1/2 and *S*=3/2 states are degenerate if separately optimized in a self-consistent manner. However, when using the *S*=3/2 state as a reference state, the spin-flip excitation energies to the *S*=1/2 ground state are non-zero. Interestingly, the spin-flip calculations indicate that there are two additional states very close in energy around the crossing region. For clarity, these states are not depicted in Figure 3.5, however, a complete picture is provided in the appendix, 3A.4.1.

The product state energy profile of **2** (green line in Figure 3.5, bottom panel) features a significant jump around a reaction coordinate value of ~0.5 Å. This is because, initially the lowest *S*=3/2 state in this system has two unpaired electrons on the catalyst and one unpaired electron on the NDI, while later in the reaction path, the state with one unpaired electron on the catalyst and two on the NDI is favourable. The observed discontinuity in the product state of **2** (Figure 3.5, bottom panel, green line) is thus a consequence of the changing nature of the reference *S*=3/2 state. Nevertheless, the region of near degeneracy between reactant and product states is still well described by this reference state. Tables with the spin configurations on the WOC and NDI part of the complexes, and the spin orbital transitions associated with the excitations to the reactant and product states are provided in the appendix, 3A.4.2 and 3A.4.3.

Our results show that, for both systems, the electron transfer process can be described as population transfer between two electronically well characterized reactant and product states. TDDFT calculations show that this charge transfer state is optically dark, therefore, once populated it is unlikely that the system would relax to the ground state via a radiative pathway. As shown schematically in Figure 3.6, one could excite the system to one of the bright, higher lying excited states, after which the system could relax to the charge transfer state (*S*=1/2 ES in Figure 3.6). Our calculations show that the charge transfer state has a gradient in the direction of the PCET product, suggesting that this could lead to a barrierless, fast process. Further research using non-adiabatic molecular dynamics could shed light on excited state relaxation pathways.

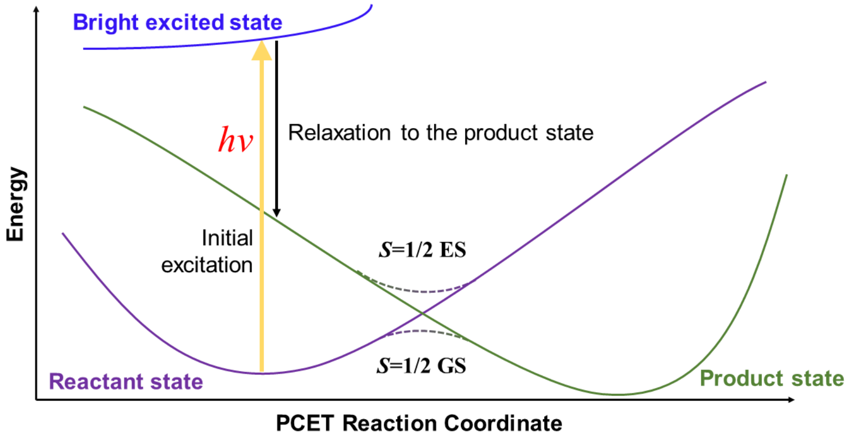

Figure 3.6. *Schematic depiction of the hypothetical laser pump scheme. An initial, appropriately tuned laser pulse populates a bright excited state. The system then relaxes to the dark product state, either via a radiative or a non-radiative decay pathway. If this process is fast enough, subsequent relaxation along the non-adiabatic product state energy surface could then result in formation of the desired PCET product.*

3.4 Conclusion

This work computationally explores the excited state potential energy surfaces of two water oxidation catalyst-dye systems, which can be used as a module in a DS-PEC device. Using static DFT calculations, an Intrinsic Reaction Coordinate path was computed for the rate limiting step in the photocatalytic cycle of both complexes. By calculating the spin density along the obtained reaction coordinate, it was possible to follow precisely at what stage the electron transfer process takes place. Subsequently, TDDFT was employed to gain insights into the excited state potential energy profile along the obtained reaction coordinates.

Two approaches are discussed which could exploit the observed potential energy profiles to accelerate the PCET step. Earlier works suggest that vibronic coupling between the reactant and product states could be facilitated by thermal activation of a torsional mode at the catalyst-dye interface. The normal frequency associated with such a mode can be tuned by chemical design and synthesis to match the energy gap between the ground and excited state, facilitating a deterministic non-adiabatic pathway from the reactant to the product. Our calculations show that indeed, around the transition state for PCET, two electronic states have an energy gap that is comparable to the energy associated with typical nuclear vibrational modes in molecules. Alternatively, the PCET rate could be enhanced by populating the charge transfer (CT) state with an appropriately tuned laser pulse sequence. We propose a scheme in which first a higher lying bright state is populated through irradiating the sample with an appropriately tuned laser pulse. If in a subsequent step, relaxation to the charge transfer state is competitive against other decay pathways, this could trigger a photo-induced proton coupled electron transfer process. TDDFT calculations suggest that radiative decay to the ground state is unlikely once the CT state is populated. Our calculations establish a qualitative view of the excited state energy surfaces involved in PCET reactions in realistic catalyst-dye complexes, showing that photo-initiation is feasible for the bidirectional PCET that occurs during the water oxidation process.

3.5 Experimental Section

All structure optimizations and (SF-) TD-DFT calculations were performed within the AMS2020 program by SCM.[59] Structures were optimized using the OPBE functional.[60] A triple-ζ polarized (TZP) Slater-type basis set was employed with a small core for all atoms with the scalar zeroth order regular approximation (ZORA) to account for relativistic effects.[61] The solvation of the complexes in water was modelled by the implicit conductor like screening model (COSMO).[62,63] Vibrational analysis was performed for verification of the local minima and saddle points. We note that the used transition state for 2 contained an additional imaginary frequency of -0.004 eV, corresponding to a soft mode in the ligand backbone. Despite numerous attempts to optimize this mode, it remained present in the final structure.

Ground and excited state energies of the obtained structures were then re-evaluated at the B3LYP/TZ2P level of theory without a frozen core and including COSMO water solvation.[64–67] The Tamm-Dancoff approximation was applied for the calculation of excitation energies within the TDDFT framework.[68] This was also the level of theory at which the spin densities were examined. TDDFT calculations were also performed with the long-range separated hybrid CAM-B3LYP and wB97-X functionals (see appendix, 3A.1.2 and 3A.1.3).[69,70] Although, these functionals reproduce the same HOMO and LUMO orbitals as B3LYP, the specific HOMO-LUMO transition, associated with the reactant to product state excitation, was not recovered by the subsequent TDDFT calculations. Therefore, it was decided to discuss the B3LYP results in the article.

3.6 References

[1] UNFCCC. Conference of the Parties (COP), *Adoption of the Paris Agreement. Proposal by the President.* **2015**, *21932*, 32.

[2] M. Grätzel, *Nature.* **2001**, *414*, 338–344.

[3] R. L. Purchase, H. J. M. De Groot, *Interface Focus* **2015**, *5*, 1–16.

[4] S. Ardo, D. Fernandez Rivas, M. A. Modestino, V. Schulze Greiving, F. F. Abdi, E. Alarcon Llado, V. Artero, K. Ayers, C. Battaglia, J. P. Becker, D. Bederak, A. Berger, F. Buda, E. Chinello, B. Dam, V. Di Palma, T. Edvinsson, K. Fujii, H. Gardeniers, H. Geerlings, S. M. Hashemi, S. Haussener, F. Houle, J. Huskens, B. D. James, K. Konrad, A. Kudo, P. P. Kunturu, D. Lohse, B. Mei, E. L. Miller, G. F. Moore, J. Muller, K. L. Orchard, T. E. Rosser, F. H. Saadi, J. W. Schüttauf, B. Seger, S. W. Sheehan, W. A. Smith, J. Spurgeon, M. H. Tang, R. Van De Krol, P. C. K. Vesborg, P. Westerik, *Energy Environ. Sci* **2018**, *11*, 2768–2783.

[5] J. D. Blakemore, R. H. Crabtree, G. W. Brudvig, *Chem. Rev.* **2015**, *115*, 12974–13005.

[6] S. Ye, C. Ding, M. Liu, A. Wang, Q. Huang, C. Li, *Adv. Mater.* **2019**, *31*, 1902069.

[7] L. H. Zhang, S. Mathew, J. Hessels, J. N. H. Reek, F. Yu, *ChemSusChem.* **2021**, *14*, 234–250.

[8] D. W. Shaffer, Y. Xie, J. J. Concepcion, *Chem. Soc. Rev.* **2017**, *46*, 6170–6193.

[9] J. J. Concepcion, J. W. Jurss, J. L. Templeton, T. J. Meyer, *J. Am. Chem. Soc.* **2008**, *130*, 16462–16463.

[10] H. Wang, E. Mijangos, S. Ott, A. Thapper, *Angew. Chem. Int. Ed.* **2014**, *1*, 14499–14502.

[11] J. M. De Ruiter, R. L. Purchase, A. Monti, C. J. M. Van Der Ham, M. P. Gullo, K. S. Joya, M. D'Angelantonio, A. Barbieri, D. G. H. Hetterscheid, H. J. M. De Groot, F. Buda, *ACS Catal.* **2016**, *6*, 7340–7349.

[12] T. Nakazono, A. R. Parent, K. Sakai, *Chem. Comm.* **2013**, *49*, 6325.

[13] L. Duan, F. Bozoglian, S. Mandal, B. Stewart, T. Privalov, A. Llobet, L. Sun, *Nat. Chem.* **2012**, *4*, 418–423.

[14] J. Yang, L. Wang, S. Zhan, H. Zou, H. Chen, M. S. G. Ahlquist, L. Duan, L. Sun, *Nat. Commun.* **2021**, *12*, 373.

[15] D. Wang, J. T. Groves, *Proc. Natl. Acad. Sci. U. S. A.* **2013**, *110*, 15579–15584.

[16] S. W. Gersten, G. J. Samuels, T. J. Meyer, *J. Am. Chem. Soc.* **1982**, *104*, 4029–4030.

[17] B. Zhang, S. Zhan, T. Liu, L. Wang, A. Ken Inge, L. Duan, B. J. J. Timmer, O. Kravchenko, F. Li, M. S. G. Ahlquist, L. Sun, *J. Energy Chem.* **2021**, *54*, 815–821.

[18] J. Hessels, R. J. Detz, M. T. M. Koper, J. N. H. Reek, *Chem. Eur. J.* **2017**, *23*, 16413–16418.

[19] M. J. Craig, G. Coulter, E. Dolan, J. Soriano-López, E. Mates-Torres, W. Schmitt, M. García-Melchor, *Nat. Commun.* **2019**, *10*, 4993.

[20] S. Hammes-Schiffer, *Acc. Chem. Res.* **2001**, *34*, 273–281.

[21] J. Y. Fang, S. Hammes-Schiffer, *J. Chem. Phys.* **1997**, *107*, 5727–5739.

[22] C. J. Gagliardi, B. C. Westlake, C. A. Kent, J. J. Paul, J. M. Papanikolas, T. J. Meyer, *Coord. Chem. Rev.* **2010**, *254*, 2459–2471.

[23] P. Goyal, C. A. Schwerdtfeger, A. V. Soudackov, S. Hammes-Schiffer, *J. Phys. Chem. B.* **2015**, *119*, 2758–2768.

[24] R. E. Warburton, A. V. Soudackov, S. Hammes-Schiffer, *Chem. Rev.* **2022**, *122*, 10599−10650.

[25] Y. Shao, J. M. De Ruiter, H. J. M. De Groot, F. Buda, *J. Phys. Chem. C.* **2019**, *123*, 21403–21414.

[26] Y. Shao, H. J. M. de Groot, F. Buda, *ChemSusChem.* **2021**, *14*, 479–486.

[27] E. J. Rabe, K. L. Corp, A. L. Sobolewski, W. Domcke, C. W. Schlenker, *J. Phys. Chem. Lett.* **2018**, *9*, 6257–6261.

[28] J. J. Concepcion, M. K. Brennaman, J. R. Deyton, N. V. Lebedeva, M. D. E. Forbes, J. M. Papanikolas, T. J. Meyer, *J. Am. Chem. Soc.* **2007**, *129*, 6968–6969.

[29] F. Weber, J. C. Tremblay, A. Bande, *J. Phys. Chem. C.* **2020**, *124*, 26688–26698.

[30] J. C. Lennox, D. A. Kurtz, T. Huang, J. L. Dempsey, *ACS Energy Lett.* **2017**, *2*, 1246–1256.

[31] J. Leier, N. C. Michenfelder, A. N. Unterreiner, M. Olzmann, *Mol. Phys.* **2021**, *119*, e1975051.

[32] K. L. Corp, E. J. Rabe, X. Huang, J. Ehrmaier, M. E. Kaiser, A. L. Sobolewski, W. Domcke, C. W. Schlenker, *J. Phys. Chem. C.* **2020**, *124*, 9151–9160.

[33] X. Huang, W. Domcke, *J. Phys. Chem. A* **2021**, *125*, 9917–9931.

[34] J. P. Menzel, M. Kloppenburg, J. Belić, H. J. M. de Groot, L. Visscher, F. Buda, *J. Comput. Chem.* **2021**, *42*, 1885–1894.

[35] L. Deng, T. Ziegler, L. Fan, *J. Chem. Phys.* **1993**, *99*, 3823–3835.

[36] L. Deng, T. Ziegler, *Int. J. Quantum Chem.* **1994**, *52*, 731–765.

[37] F. Wang, T. Ziegler, *J. Chem. Phys.* **2004**, *121*, 12191–12196.

[38] F. Wang, T. Ziegler, *J. Chem. Phys.* **2005**, *122*, 074109.

[39] Y. Shao, M. Head-Gordon, A. I. Krylov, *J. Chem. Phys.* **2003**, *118*, 4807–4818.

[40] N. Minezawa, M. S. Gordon, *J. Phys. Chem. A.* **2009**, *113*, 12749–12753.

[41] M. Huix-Rotllant, B. Natarajan, A. Ipatov, C. Muhavini Wawire, T. Deutsch, M. E. Casida, *Phys. Chem. Chem. Phys.* **2010**, *12*, 12811–12825.

[42] Z. Rinkevicius, O. Vahtras, H. Ågren, *J. Chem. Phys.* **2010**, *133*, 114104.

[43] E. Salazar, S. Faraji, *Mol. Phys.* **2020**, *118*, e1764120.

[44] K. G. Moghaddam, G. Giudetti, W. Sipma, S. Faraji, *Phys. Chem. Chem. Phys.* **2020**, *20*, 26944–26954.

[45] H. Li, X. Gong, H. Ni, P. Lu, X. Luo, J. Wen, Y. Yang, X. Qian, Z. Sun, J. Wu, *J. Phys. Chem. Lett.* **2022**, 5881–5893.

[46] B. C. Paulus, S. L. Adelman, L. L. L. Jamula, J. K. K. McCusker, *Nature.* **2020**, *582*, 214–218.

[47] J. Nyhlén, L. Duan, B. Åkermark, L. Sun, T. Privalov, *Angew. Chem. Int. Ed.* **2010**, *49*, 1773–1777.

[48] C. Röger, F. Würthner, *J. Org. Chem.* **2007**, *72*, 8070–8075.

[49] N. Sakai, J. Mareda, E. Vauthey, S. Matile, *Chem. Commun.* **2010**, *46*, 4225.

[50] M. Al Kobaisi, S. V. Bhosale, K. Latham, A. M. Raynor, S. V. Bhosale, *Chem. Rev.* **2016**, *116*, 11685–11796.

[51] J. Belić, B. van Beek, J. P. Menzel, F. Buda, L. Visscher, *J. Phys. Chem. A.* **2020**, *124*, 6380–6388.

[52] A. Monti, J. M. De Ruiter, H. J. M. De Groot, F. Buda, *J. Phys. Chem. C.* **2016**, *120*, 23074–23082.

[53] C. J. D. T. von Grotthuss, *Ann. Chim. (Paris)* **1806**, *58*, 54–74.

[54] N. Agmon, *Chem. Phys. Lett.* **1995**, *244*, 456–462.

[55] J. Baker, A. Scheiner, J. Andzelm, *Chem. Phys. Lett.* **1993**, *216*, 380–388.

[56] R. L. Martin, *J. Chem. Phys.* **2003**, *118*, 4775–4777.

[57] R. J. Cave, M. D. Newton, *Chem. Phys. Lett.* **1996**, *249*, 15–19.

[58] R. J. Cave, M. D. Newton, *J. Chem. Phys.* **1997**, *106*, 9213–9226.

[59] AMS2021.101, SCM, Theoretical Chemistry. Vrije Universiteit: Amsterdam, The Netherlands. https://www.scm.com.

[60] M. Swart, A. W. Ehlers, K. Lammertsma, *Mol. Phys.* **2004**, *102*, 2467–2474.

[61] E. Van Lenthe, *J. Chem. Phys.* **1999**, *110*, 8943–8953.

[62] A. Klamt, *J. Phys. Chem.* **1995**, *99*, 2224–2235.

[63] A. Klamt, V. Jonas, *J. Chem. Phys.* **1996**, *105*, 9972–9981.

[64] A. D. Becke, *Phys. Rev. A.* **1988**, *38*, 3098.

[65] A. D. Becke, *J. Chem. Phys.* **1993**, *98*, 1372–1377.

[66] S. H. Vosko, L. Wilk, M. Nusair, *Can. J. Phys.* **1980**, *58*, 1200–1211.

[67] P. J. Stephens, F. J. Devlin, C. F. Chabalowski, M. J. Frisch, *J. Phys. Chem.* **1994**, *98*, 11623–11627.

[68] S. Hirata, M. Head-Gordon, *Chem. Phys. Lett.* **1999**, *314*, 291–299.

[69] T. Yanai, D. P. Tew, N. C. Handy, *Chem. Phys. Lett.* **2004**, *393*, 51–57.

[70] J.-D. Chai, M. Head-Gordon, *J. Chem. Phys.* **2008**, *128*, 084106.

3A. Appendix

3A.1 Additional TDDFT calculations

3A.1.1 TDDFT results for the C-bound [Ru(bda)(pic)$_2$(H$_2$O)]$^+$-NDI complex

The obtained *S*=1/2 GS and ES energy profiles of the carbon bound WOC-NDI complex look similar to the profiles obtained for **1**. Only in the region of the transition state, two TDDFT calculations do not find the HOMO-LUMO excitation that describes the excited state PES of interest.

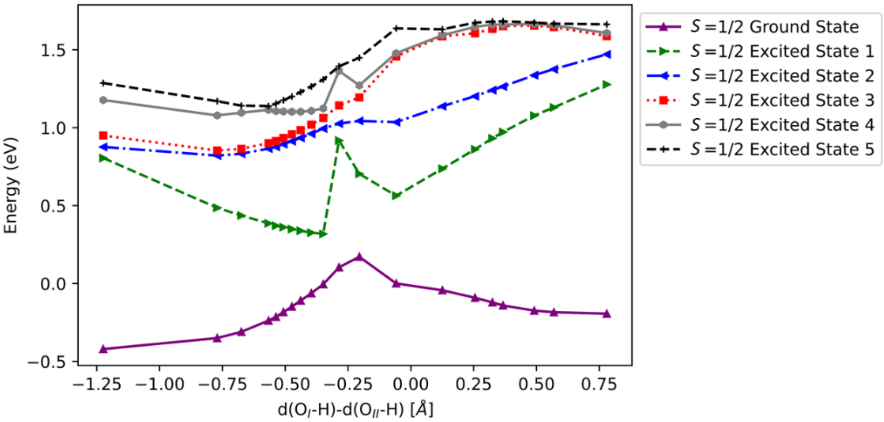

Figure 3A.1. *Ground and excited state energy profile for the carbon bound [Ru(bda)(pic)2]+ (bda = 2,2'-bipyridine-6,6'-dicarboxylic acid, pic = 4-picoline) 2,6-diethoxy-1,4,5,8-diimidenapthalene complex. Excitation energies are calculated at the B3LYP/TZ2P/COSMO level of theory.*

3A.1.2 TDDFT results on 1 using the CAM-B3LYP functional

Calculations with the CAM-B3LYP functional do not always converge to the proper electronic state, especially in the region of the transition state. For the entire IRC path, the CAM-B3LYP TDDFT calculations do not find the charge transfer HOMO-LUMO excitation that was investigated in this article.

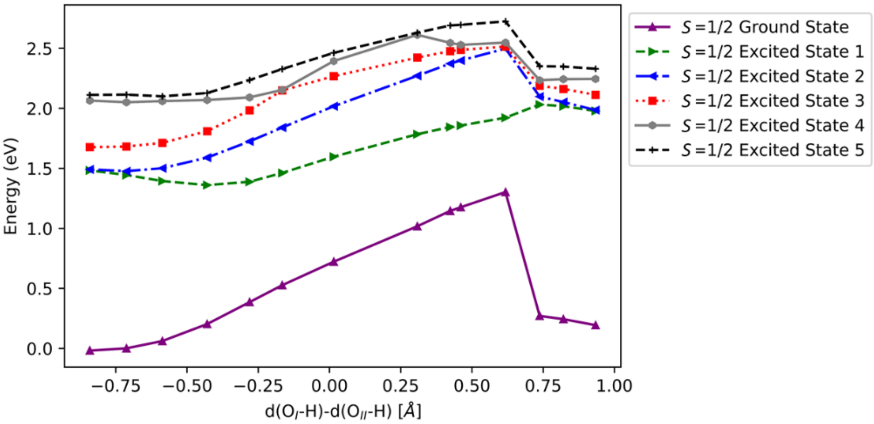

Figure 3A.2. *Ground and excited states energy profile for* ***1****. Excitations calculated at the CAM-B3LYP/TZ2P/COSMO level of theory.*

3A.1.3 TDDFT results on 1 using the wB97-X functional

The calculations with the wB97-X functional do recover for all investigated geometries along the PCET IRC path the proper electronic ground state. However, also for this range separated functional, the investigated HOMO-LUMO excitations are not recovered in the performed TDDFT calculations.

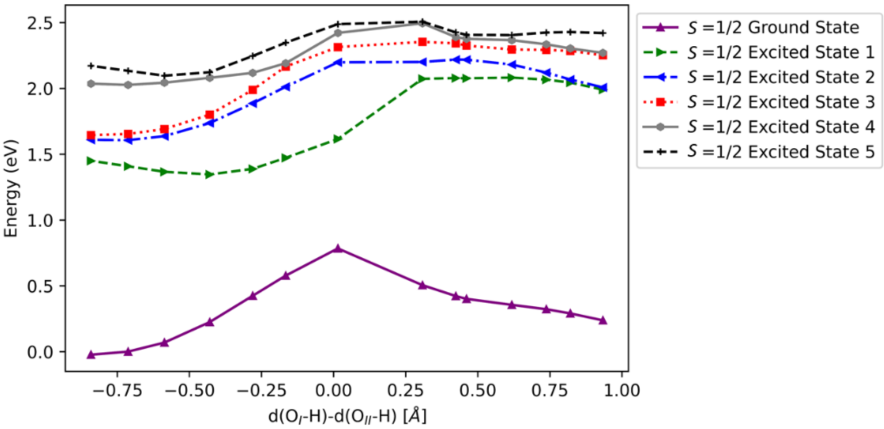

Figure 3A.3. *Ground and excited states energy profile for* ***1****. Excitations calculated at the wB97X/TZ2P/COSMO level of theory.*

3A.1.4 Excited state geometry optimization of 1

In addition to the excited state analysis on the ground state IRC reaction path, also an excited state geometry relaxation from the Franck-Condon point was performed for **1**. The optimized geometries at the Franck-Condon point, the PCET transition state and the $S = ½$ excited state are visualized in Figure 3A.4 (top). The first optimization steps from the Franck-Condon point mainly affected the orientation of the dye fragment with respect to the WOC. In the subsequent relaxation steps, the hydroxide oxygen-proton distance (O_I-H) is elongated from 0.99 Å to 1.08 Å and the distance from the hydroxide proton to the nucleophilic water oxygen atom (O_{II}-H) is shortened significantly from 1.83 Å to 1.42 Å (see table 3A.1). It was found that the same reaction coordinate that was used to describe the ground state PCET reaction could also be used to track the excited state geometry optimization. This geometry optimization supports the finding that the excited state has a gradient in the direction of the product of the PCET reaction. The S=1/2 excited state and ground state energy profile along the d(O_I-H)- d(O_{II}-H) reaction coordinate is plotted in Figure 3A.4 (bottom).

The excited state geometry optimization was performed at the same level of theory as the excited state calculations from the main paper, except for the basis set, which was scaled down from TZ2P to TZP quality in order to make the computation more efficient. The geometry was optimized up to an energy convergence of $1\text{x}10^{-3}$ H Bohr^{-1}, a max gradient convergence of $1\text{x}10^{-3}$ H Bohr^{-1} and a root mean square gradient convergence of $2{\cdot}10^{-4}$ H Bohr^{-1}.

Table 3A.1. Distances of the dissociating and forming O-H bonds at Franck-Condon point, transition state and optimized excited state structures.

Structure	O_I – H distance (Å)	O_{II} – H distance (Å)
Franck-Condon point	0.991	1.832
Transition State	1.219	1.204
Optimized Excited State	1.077	1.422

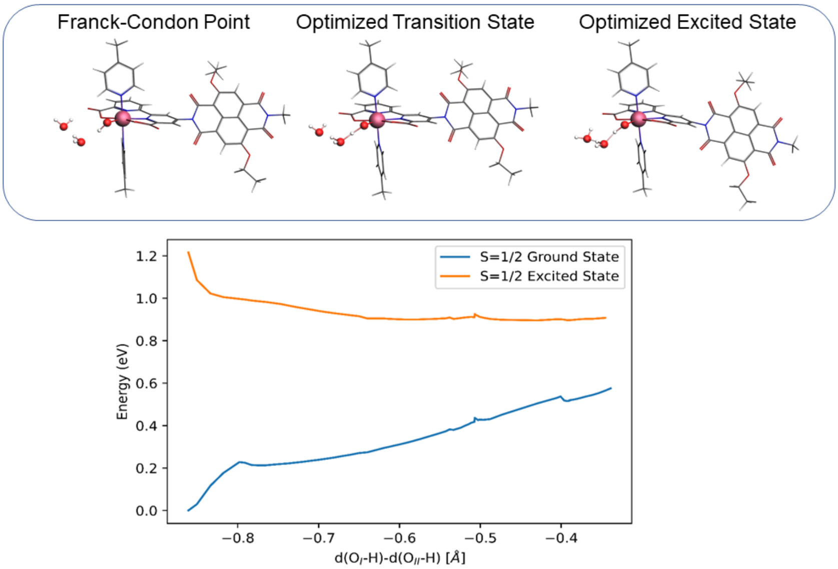

Figure 3A.4. *On top, the optimized structures of* ***1*** *at the Franck-Condon point, at the optimized transition state and at the optimized excited state. On the bottom, a plot of the ground and excited states energy profile along an excited state geometry optimization for* ***1****. The calculation was performed at the B3LYP/TZP/COSMO level of theory.*

3A.2.1 Obtaining the IRC paths

As a starting point for the investigation, an unconstrained geometry optimization was carried out of the two model systems. Performing a series of geometry optimizations then allowed for the search of a single normal mode that describes either the proton coupled electron transfer reaction from the Ru(IV)-OH species to form the Ru(V)=O intermediate (see Figure 3.1, Reaction 1) or O-O bond formation between the Ru(IV)=O intermediate and a H_2O molecule (see Figure 3.1, reaction 2). By performing a hessian calculation on a structure close to the TS, the normal modes corresponding to these geometric rearrangements were obtained. A transition state (TS) for each WOC-dye complex was located by optimization of the found normal mode without any constraints. Even though at this stage the constraints were lifted, no large structural changes were observed for the chain of water molecules in either system. Once a TS was located and characterized by a frequency calculation, the IRC method was employed to obtain the steepest descent path in mass-weighed coordinates from the TS to the reactant and product complexes. In the case of complex 2, the range of the reaction coordinate was extended by performing a series of 10 constrained optimizations with a O-O distance between 2.05 and 3.14 Å. The xyz trajectory files of the obtained IRC paths are provided as supplementary materials to the original publication, IRC_traj_1.xyz and IRC_traj_2.xyz.[1]

3A.2.2 Ground state IRC reaction paths for 1 and 2

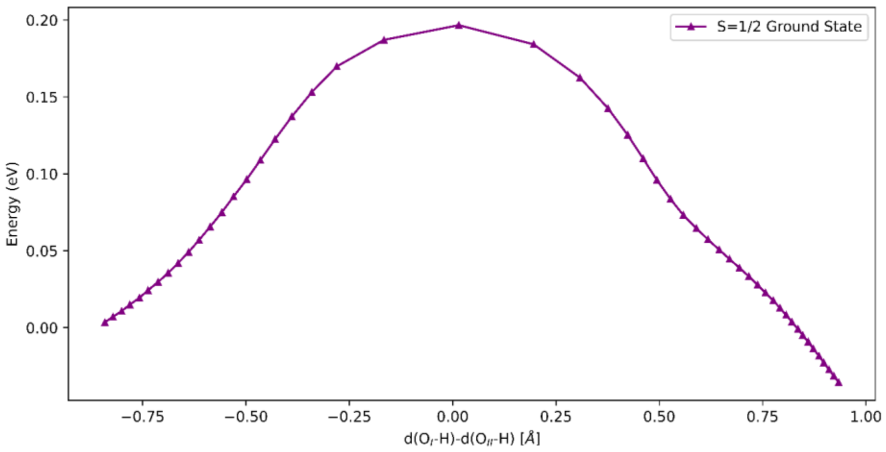

Figure 3A.5. *Ground state energy profile for* ***1****, as obtained from the IRC calculation performed at the OPBE/TZP/COSMO level of theory.*

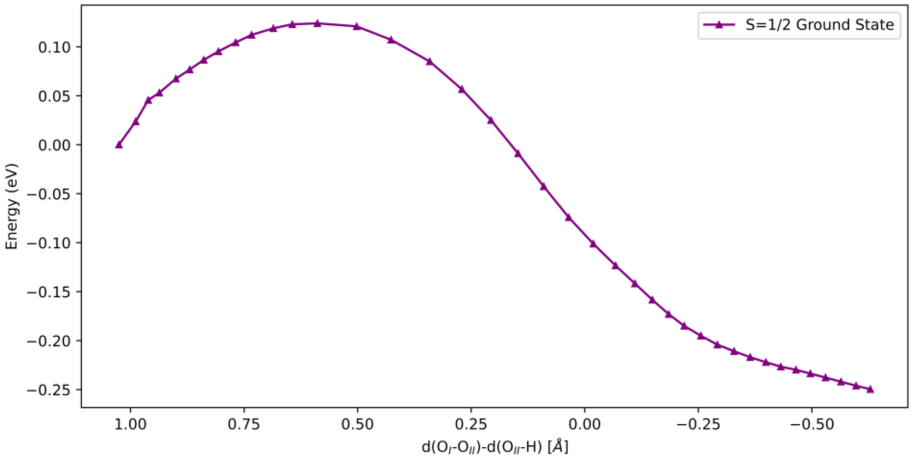

Figure 3A.6. *Ground state energy profile for* ***2****, as obtained from the IRC calculation performed at the OPBE/TZP/COSMO level of theory.*

3A.2.3 Expectation value for the $\hat{S}^2$ operator along the PCET reaction coordinate for 2

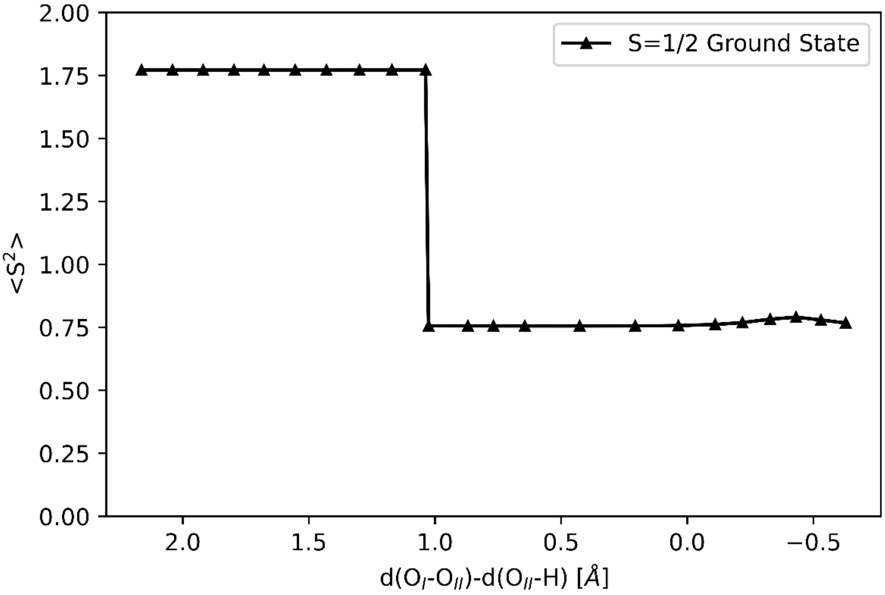

Figure 3A.7. *Expectation value of the $\hat{S}^2$ operator along the PCET reaction coordinate for **2**.*

3A.3.1 Excitation energies and oscillator strengths of 1 and 2 at initial and final structures of the investigated reaction path

Table 3A.2. Excitation energies and oscillator strengths for complex 1 in the initial and final geometry on the IRC path. Excitations are computed at the B3LYP/TZ2P/COSMO level of theory within the Tamm-Dancoff TDDFT framework.

	Reactant structure		Product structure	
Number	Excitation energies (eV)	Oscillator strengths	Excitation Energies (eV)	Oscillator strengths
1	1.15	0.0001	1.41	0.0002
2	1.30	0.0002	1.69	0.0012
3	1.36	0.0004	1.76	0.0089
4	1.60	0.0000	1.79	0.0000
5	1.60	0.0000	1.84	0.0001
6	1.76	0.0000	1.93	0.0000
7	1.78	0.0171	2.08	0.0003
8	1.78	0.0036	2.16	0.0000
9	1.85	0.0000	2.33	0.0003

Table 3A.3. Excitation energies and oscillator strengths for complex 2 in the initial and final geometry on the IRC path. Excitations are computed at the B3LYP/TZ2P/COSMO level of theory within the Tamm-Dancoff TDDFT framework.

Reactant structure		Product structure	
Excitation energies (eV)	Oscillator strengths	Excitation Energies (eV)	Oscillator strengths
1.28	0.0017	1.32	0.0000
1.36	0.0008	1.44	0.0016
1.56	0.0193	1.64	0.0015
1.57	0.0008	1.75	0.0072
1.63	0.1069	2.03	0.0036
1.82	0.0101	2.27	0.0001
1.88	0.1032	2.36	0.0277
1.94	0.0060	2.55	0.0055
2.11	0.0006	2.63	0.0034

3A.3.2 Transition dipole moment, dipole moment, excitation energy and the H_{ab} coupling element of 1 and 2 along the investigated reaction path

In order to gain further insights into the coupling between the reactant and product states, the electronic coupling elements were calculated following the Generalized Mulliken-Hush ansatz.[2,3]

$$V_{\mathrm{et}} = \frac{\Delta E_{12}\,|\vec{\mu}_{12}|}{[(\vec{\mu}_{11} - \vec{\mu}_{22})^2 + 4(\vec{\mu}_{12})^2]^{\frac{1}{2}}}$$

In this equation, ΔE_{12} and μ_{12} are the vertical excitation energy and transition dipole moment between states 1 and 2, and μ_{11} and μ_{22} are the dipole moments for state 1 and 2, respectively. In the AMS2020 program, ΔE_{12}, μ_{11} and μ_{12} are readily obtained from an unrestricted open-shell TDDFT calculation. However, as of yet, it is not possible to calculate the excited state dipole moment, μ_{22}. Therefore, we approximate the μ_{22} parameter as the dipole moment of the first structure along the reaction coordinate, where the electronic ground state corresponds to the product state (and vice-versa for the coupling after the PCET event). For **1**, the coupling remains relatively constant. Along the entire reaction path a value around $1.5 \cdot 10^{-4}$ H is found (corresponding to 32 cm^{-1}). For **2**, the calculated matrix elements do change significantly along the reaction coordinate, particularly the first four reactant structures show a higher coupling around $4.5 \cdot 10^{-4}$ H (corresponding to 99 cm^{-1}) . These structures were not part of the initial IRC reaction path, but correspond the constraint geometry optimizations that were used to elongate the reaction path. Likely, this caused larger distortions in the geometry, resulting in a larger changes in the parameters that were used to calculate the coupling. The Larger coupling in these structures is caused mainly by a larger transition dipole moment, as can be seen in Figure 3A.8.

The magnitude of μ_{12} and μ_{11} vectors, the electronic excitation energy and the calculated electronic coupling elements along the investigated reaction coordinate for **1** and **2** are presented in figures 3A.8 and 3A.9.

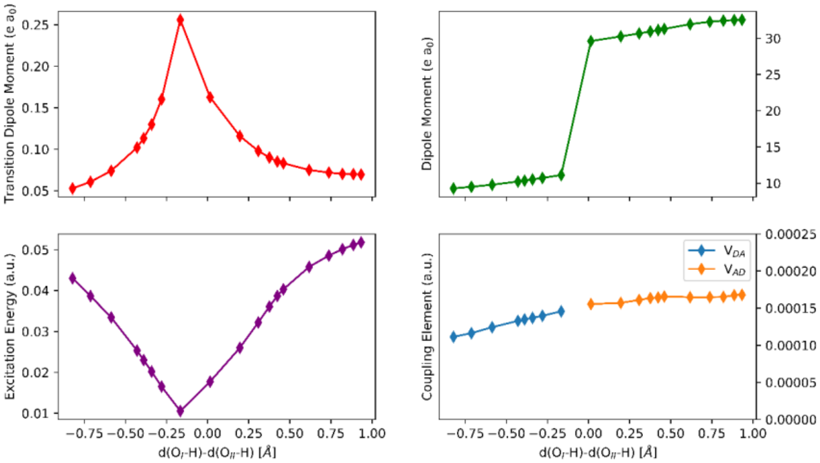

Figure 3A.8. *Calculated transition dipole moment between S=1/2 ground and excited state (upper left panel), S=1/2 ground state dipole moment (upper right panel) and the first excitation energy (lower left panel) along the investigated reaction coordinate for* ***1****. The electronic coupling between reaction and product states (first half of the reaction, in blue) and product and reactant states (second half of the reaction, orange) are plotted in the bottom right panel.*

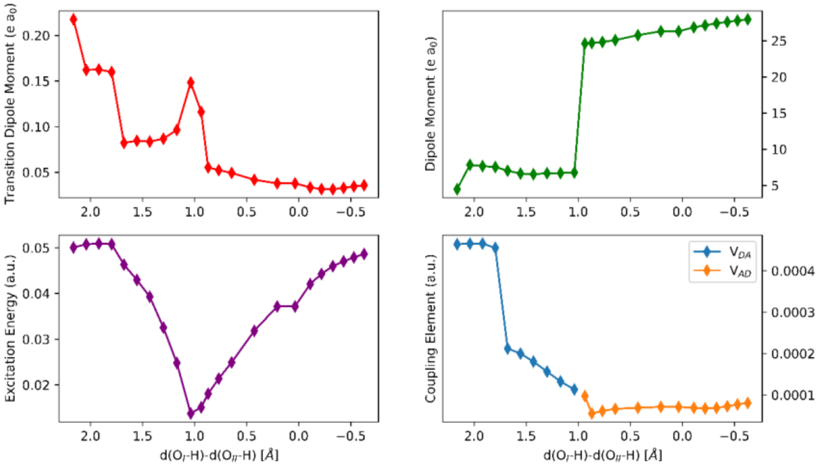

Figure 3A.9. *Calculated transition dipole moment between S=1/2 ground and excited state (upper left panel), S=1/2 ground state dipole moment (upper right panel) and the first excitation energy (lower left panel) along the investigated reaction coordinate for* ***2****. The electronic coupling between reaction and product states (first half of the reaction, in blue) and product and reactant states (second half of the reaction, orange) are plotted in the bottom right panel.*

3A.4.1 SF-TDDFT results for 2

SF-TDDFT calculations on **2** reveal that at the beginning of the reaction path (longer O-O distance), previously not found electronic states are present beneath the doublet product state that was displayed in Figure 3.3. By analyzing the spin-orbital transitions associated with each excitation, the diabatic reactant and product states could be assigned at each frame in the IRC path. The other excitations all featured significant mixed orbital character, making it hard to consistently assign excited states for different frames.

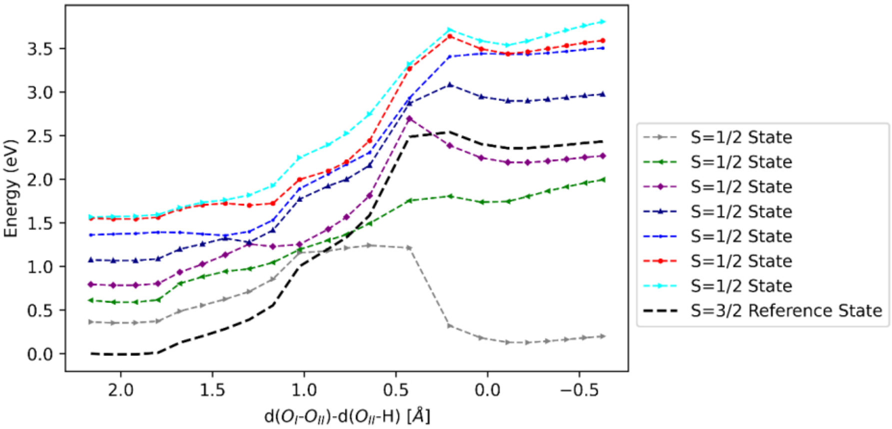

Figure 3A.10. *Spin-flip TDDFT results for* **2**. *Excitations calculated at the B3LYP/TZ2P/COSMO level of theory.*

3A.4.2 Interpretation of the spin-orbital transitions in the SF-TDDFT calculations for 1

The S=1/2 ground state and S=1/2 excited states were computed as spin-flip excitations from the S=3/2 reference state (^{4}QRS). The reactant and product states can be identified by analyzing the spin-orbitals associated with the spin-flip transitions. In Table 3A.4 the interpretation of the calculated transitions is provided. Note that the indicated ruthenium d orbitals actually contain large oxygen p-orbital character as well as contributions from the ligand π-system (see Figure 3A.11). The HOMO and LUMO labels on the NDI refer to the HOMO and LUMO in the S=3/2 reference electronic state, not the HOMO and LUMO of the S=1/2 diabatic reactant and product states.

Table 3A.4. Spin configurations of different diabatic reactant and product states on WOC and Dye for complex 1 used in the SF-TDDFT. See also Figure 3A.11 for the visualization of the orbitals.

Diabatic state	Spin configuration on WOC	Spin configuration on NDI	Transition	Total spin
^{4}QRS (quartet reference state)	$d_{xy}(\alpha)$, $d_{yz}(\alpha)$	$\mathrm{NDI_{HOMO}}(\alpha)$	Reference state	3/2
^{2}RS (reactant state)	$d_{yz}(\alpha)$, $d_{xz}(\beta)$	$\mathrm{NDI_{HOMO}}(\alpha)$	$d_{xy}(\alpha) \rightarrow d_{xz}(\beta)$	1/2
^{2}PS (product state)	$d_{yz}(\alpha)$	$\mathrm{NDI_{HOMO}}(\alpha)$ $\mathrm{NDI_{LUMO}}(\beta)$	$d_{xy}(\alpha)$ $\rightarrow \mathrm{NDI_{LUMO}}(\beta)$	1/2

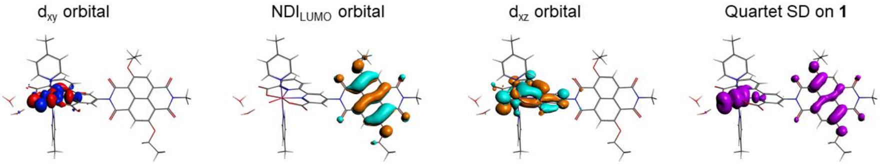

Figure 3A.11. *Orbitals involved with the spin-flip excitations to the diabatic reactant and product states and the spin density of the quartet reference state. Isosurface values are set at 0.03 for the visualized orbitals and at 0.002 for the spin density.*

3A.4.3 Interpretation of the spin-orbital transitions in the SF-TDDFT calculations for 2

Table 3A.5. Spin configurations of different diabatic reactant and product states on WOC and Dye for **2** before change of reference state

Diabatic state	Spin configuration on WOC	Spin configuration on NDI	Transition	Total spin
^{4}QRS (quartet reference state)	$d_{xz}(\alpha)$, $d_{yz}(\alpha)$	$\mathrm{NDI}_{\mathrm{HOMO}}(\alpha)$	Reference state	3/2
^{2}RS (reactant state)	$d_{xz}(\alpha)$, $d_{yz}(\beta)$	$\mathrm{NDI}_{\mathrm{LUMO}}(\alpha)$	$d_{xz}(\alpha) \rightarrow d_{yz}(\beta)$	1/2
^{2}PS (product state)	$d_{xz}(\alpha)$	$\mathrm{NDI}_{\mathrm{HOMO}}(\alpha)$ $\mathrm{NDI}_{\mathrm{LUMO}}(\beta)$	$d_{xz/yz}(\alpha)$ $\rightarrow \mathrm{NDI}_{\mathrm{LUMO}}(\beta)$	1/2

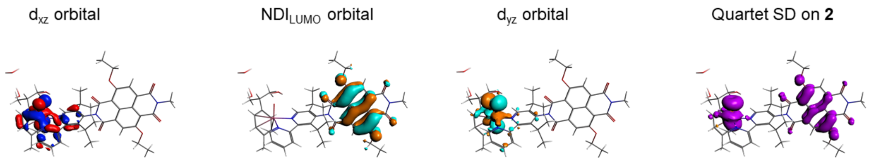

Figure 3A.12. *Orbitals involved with the spin-flip excitations to the diabatic reactant and product states and the spin density (SD) of the quartet reference state for the first frames. Isosurface values are set at 0.03 for the visualized orbitals and at 0.002 for the spin density.*

Table 3A.6. Spin configurations of different diabatic reactant and product states on WOC and Dye for 2 after change of reference state

Diabatic state	Spin configuration on WOC	Spin configuration on NDI	Spin transition	Total spin
^{4}QRS (quartet reference state)	Ru-d$_{xz/yz}$(α)	NDI$_{\mathrm{HOMO-1}}$(α), NDI$_{\mathrm{HOMO}}$(α)	Reference state	3/2
^{2}RS (reactant state)	Ru-d$_{xz/yz}$(α), O-p$_{x/y}$(α)	NDI$_{\mathrm{LUMO}}$(β)	NDI$_{\mathrm{HOMO}}$(α) →d$_{yz/xz}$(β)	1/2
^{2}PS (product state)	Ru-d$_{xz/yz}$(α)	NDI$_{\mathrm{HOMO-1}}$(α), NDI$_{\mathrm{LUMO}}$(β)	NDI$_{\mathrm{HOMO}}$(α) →NDI$_{\mathrm{LUMO}}$(β)	1/2

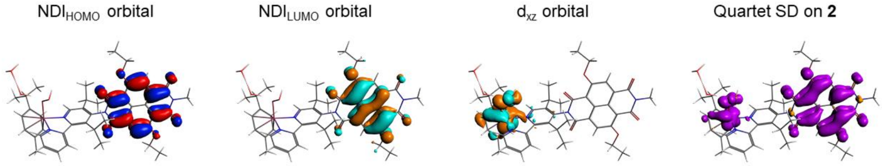

Figure 3A.13. *Orbitals involved with the spin-flip excitations to the diabatic reactant and product states and the spin density (SD) of the quartet reference state after the reference state switch. Isosurface values are set at 0.03 for the visualized orbitals and at 0.002 for the spin density.*

3A.5. References

[1] T. de Haas, H. van Overeem, H. J. M. de Groot, F. Buda, *ChemPhotoChem* **2022**, e202200274.
[2] R. J. Cave, M. D. Newton, *Chem. Phys. Lett.* **1996**, *249*, 15–19.
[3] R. J. Cave, M. D. Newton, *J. Chem. Phys.* **1997**, *106*, 9213–9226